

ARTICLE

Open Access

# Rejuvenation engineering in metallic glasses by complementary stress and structure modulation

Daniel Şopu<sup>1,2</sup>, Florian Spieckermann<sup>3</sup>, Xilei Bian<sup>4</sup>, Simon Fellner<sup>1</sup>, Jonathan Wright<sup>5</sup>, Megan Cordill<sup>1</sup>, Christoph Gämmer<sup>1</sup>, Gang Wang<sup>4</sup>, Mihai Stoica<sup>6</sup> and Jürgen Eckert<sup>1,3</sup>

## Abstract

Residual stress engineering is widely used in the design of new advanced lightweight materials. For metallic glasses, attention has been given to structural changes and rejuvenation processes. High-energy scanning X-ray diffraction strain mapping reveals large elastic fluctuations in notched metallic glasses after deformation under triaxial compression. Microindentation hardness mapping hints at a competing hardening–softening mechanism after compression and reveals the complementary effects of stress and structure modulation. Transmission electron microscopy proves that structure modulation and elastic heterogeneity distribution under room temperature deformation are related to shear band formation. Molecular dynamics simulations provide an atomistic understanding of the confined deformation mechanism in notched metallic glasses and the related fluctuations in the elastic and plastic strains. Thus, future focus should be given to stress modulation and elastic heterogeneity, which, together with structure modulation, may allow the design of metallic glasses with enhanced ductility and strain-hardening ability.

## Introduction

Given the metastable nature of metallic glasses (MGs) and the related rugged energy landscape with a wide diversity of energy barriers, the properties of this class of material are easily tunable<sup>1,2</sup>. To date, there are many methods available for altering the structures and corresponding properties of MGs<sup>3–11</sup>. Rejuvenation and relaxation are competing processes in controlling the energies of MGs toward higher and lower levels, ultimately resulting in a wide range of possible glassy states<sup>8,12</sup>. Rejuvenation of metallic glasses is usually associated with increased disorder, excess free volume (or reduced density), increased plasticity and toughness, and reduced hardness and strength<sup>9,13</sup>. However, some rejuvenation processes involving deformation protocols and

thermal treatments have revealed increases in density and hardness in some metallic glasses<sup>14–16</sup>. The observed strain-hardening behaviors in these alloys following treatment are associated with confined microplasticity and local accumulation of irreversible compressive strains<sup>17,18</sup>. Deformation by cold-rolling and shot-peening can also promote a transition from softening to hardening behavior, which can be correlated to the accumulation of compressive residual stresses that overcompensate for free volume generation and associated shear softening<sup>19,20</sup>. Highly rejuvenated MGs, such as those obtained under triaxial compression, have revealed strain hardening and a greatly enhanced ductility<sup>6,21</sup>. The exceptionally efficient strain-hardening and suppression of shear banding are associated with structural relaxation of the extremely rejuvenated MG during deformation<sup>21</sup>.

While structural rejuvenation has received much attention, there has been decreasing interest in recent years in exploring stress engineering in MGs. Due to their very low thermal conductivities and high cooling rates involved in the quenching process, MGs undergo differential cooling, and large thermal gradients are generated

Correspondence: Daniel Şopu (daniel.sopu@oaew.ac.at) or Florian Spieckermann (florian.spieckermann@unileoben.ac.at) or Xilei Bian (bianxilei@shu.edu.cn)

<sup>1</sup>Erich Schmid Institute of Materials Science, Austrian Academy of Sciences, Jahnstraße 12, 8700 Leoben, Austria

<sup>2</sup>Institut für Materialwissenschaft, Fachgebiet Materialmodellierung, Technische Universität Darmstadt, Otto-Berndt-Straße 3, 64287 Darmstadt, Germany

Full list of author information is available at the end of the article

across the samples, leading to residual stress buildup<sup>22,23</sup>. Residual stresses and stress field gradients affect shear band dynamics and the overall plastic deformation<sup>20,24</sup>, hardness<sup>23,25</sup>, and magnetic properties of MGs<sup>26</sup>. Recently, molecular dynamics (MD) simulations of stress-modulated MG heterostructures have revealed that strain hardening and tensile ductility can be attained by modulating the internal residual stress without altering the structure<sup>27</sup>.

Herein, we focus our attention on clarifying the key factors underlying the rejuvenation process under triaxial compression and distinguishing between structural heterogeneities and elastic fluctuations. By using a similar setup proposed by Pan et al.<sup>21</sup> at the European Synchrotron Radiation Facility (ESRF) Extremely Brilliant Source, we perform strain mapping of extremely deformed MG samples. This novel approach allows us to distinguish hydrostatic from deviatoric strains and to quantify structural and stress heterogeneities<sup>28,29</sup>. Transmission electron microscopy (TEM) is applied to highlight intense shear band activity during room temperature deformation. Hardness mapping with microindentation is used to emphasize the competing effects of stress and structure modulation. Finally, an atomistic understanding of the confined deformation mechanisms in a notched MG is provided by MD simulations.

## Materials and methods

### Preparation of metallic glass samples

Metallic glass with a nominal composition of Zr<sub>61</sub>Ti<sub>2</sub>Cu<sub>25</sub>Al<sub>12</sub> (at.%) was prepared by arc melting a mixture of high-purity (>99.9%) metals at least four times in a titanium-gettered high-purity argon atmosphere. Cylindrical samples with a diameter of 4.5 mm and a length of 70 mm were fabricated by suction casting into a copper mold. The structures of the glassy phases of the as-cast MG samples were ascertained by X-ray diffraction (XRD) using a Rigaku Dmax-2550 diffractometer with Cu-K $\alpha$  radiation generated at 40 kV. Specimens with a length/diameter ratio of 2 were cut from the rods by a diamond saw, and the rough surfaces of the two parallel ends were carefully polished. Notched specimens with circumferential notch dimensions (notch diameter,  $d$   $\times$  notch height,  $h$ ) of  $2.5 \times 0.5$  mm<sup>2</sup> were produced using a 0.5-mm diameter round head grooving knife at a feed rate of 0.06 mm/r in a lathe machine with a running speed of 500 r/min, followed by fine polishing and final cleaning in an ultrasonic bath. Then, the notched specimens were compressed along the cylindrical axis at room temperature using an MTS CMT5205 device at a strain rate of  $10^{-4}$  s<sup>-1</sup> until the width of the notch was reduced by  $\approx$ 40% engineering strain. Due to the notch constraint, the central zone was deformed under triaxial compression, suppressing relaxation<sup>21</sup>. The deformed specimens were

then machined along the central lateral and longitudinal planes. The longitudinal cross-sections were mechanically polished to mirror finish for the following high-energy XRD and nanoindentation experiments.

### Structural characterization

High-energy scanning XRD was used to perform strain mapping on the cross-section of the deformed specimen, which was carried out at the nanostation of beamline ID11 at ESRF. A wavelength of 0.01919 nm was used, and the beam size was focused to  $500 \times 500$  nm. The region of interest was scanned with 3500 points with a spacing of 1  $\mu$ m each in the fast scanning direction and 65 points with a spacing of 50  $\mu$ m in the slow scanning direction, leading to a total of 227,500 two-dimensional diffraction patterns recorded with an exposure time of 10 ms via an Eiger CdTe 4 M fast pixel array detector. In the fast scanning direction, 50 frames were summed to increase the signal-to-noise ratio. The newly upgraded extremely brilliant source (EBS) of ESRF allowed the measurement of half of the sample in approximately 2 h.

The data were calibrated using a CeO<sub>2</sub> reference and integrated using pyFAI software. For the evaluation of plane strains, the integration was performed in 72 azimuthal sections. The volumetric strains were evaluated using the average center of mass of the first strong diffraction maximum  $q_{\text{COM}}/q_0$  of the glassy material. The fitting procedure was reproduced for a representative diffraction pattern in Fig. S1. For the plane strains  $\varepsilon_{11}$ ,  $\varepsilon_{12}$ , and  $\varepsilon_{22}$ , the normalized center of mass of the first diffraction maximum  $q(\varphi)/q_{\text{COM}}$  was fitted using the following equation for the azimuthal angle  $\varphi$  similar to the established procedure<sup>28</sup>:

$$\varphi = \varepsilon_{11} \cos(\varphi)^2 + \varepsilon_{12} \cos(\varphi) \sin(\varphi) + \varepsilon_{22} \sin(\varphi)^2 \quad (1)$$

The high flux of EBS and new fast pixel array detectors with single photon counting ability allowed correlation of the mesoscale information occurring in the plastic deformation of the notched MG sample with the formation of individual shear bands and their interactions. Strain mapping allowed the identification and visualization of shear bands in the bulk material in 2D.

Thin lamella for scanning transmission electron microscopy (STEM) was prepared with a final thickness of 100 nm by focused ion-beam milling using a Zeiss Auriga dual-beam workstation. One lamella was taken from the middle part between the two notches of the specimen. A second lamella was taken from a position inclined by 45° with respect to the notch direction. High-angle annular dark field (HAADF) STEM images were recorded for each lamella with a spot size of 1 nm.

Macroscopic Vickers hardness maps were recorded using a universal fully automatic DuraScan70G5 laboratory ZwickRoell hardness tester. The areal distribution of indentation points was recorded in a grid of  $200 \times 200 \mu\text{m}$  with a total number of 546 indents in a matrix of  $26 \times 21$ . To avoid the influence of the elastic-plastic stress field, the indents were spaced three diagonals apart. The indentation depth of each indent was approximately  $15 \mu\text{m}$ , calculated using the  $136^\circ$  opening angle of the pyramid-shaped diamond indenter. A load of 9807 N was applied for each impression, which corresponds to the small load range of HV1.

### Molecular dynamics simulations

A qualitative and elemental atomistic picture of the confined deformation in a notched MG was provided through classical molecular dynamics simulations carried out with (Large-scale atomic/molecular massively parallel simulator) LAMMPS software<sup>30</sup>. Because no appropriate interatomic potentials exist for  $\text{Zr}_{61}\text{Ti}_2\text{Cu}_{25}\text{Al}_{12}$ ,  $\text{Cu}_{64}\text{Zr}_{36}$  MG was used as a prototype material since a reliable EAM potential was made available by Mendelev et al.<sup>31</sup>. The amorphous  $\text{Cu}_{64}\text{Zr}_{36}$  alloy structures predicted by the potential were in good agreement with X-ray diffraction data, and the potential could be reliably used to simulate the structure and properties of amorphous Cu-Zr alloys<sup>32,33</sup>.

The starting liquid structure was created by randomly distributing 968000 atoms in a box of  $111.0 \times 55.5 \times 2.5 \text{ nm}$  with periodic boundary conditions. The amorphous structure was obtained by quenching from the melt starting at 2000 K. Further details about the quenching procedure can be found in ref.<sup>34</sup>. The cooled sample was replicated twice along the  $z$ -direction, and two notches were created along the  $y$ -direction. Open boundaries in the  $y$ -direction and periodic boundaries in the  $x$ - and  $z$ -directions were applied. The time step was set to 2 fs.

Uniaxial compression simulations along the  $z$ -direction were performed on the notched MG sample under a constant engineering strain rate of  $4 \times 10^7 \text{ s}^{-1}$ . The stress along the  $x$ -direction was relaxed to allow for lateral contraction using a Nose/Hoover barostat<sup>30</sup>. A low temperature of 50 K was chosen to compensate for the very high strain rate and to guarantee a regime of localized deformation and shear band formation. The deformation mechanisms and the related structural fluctuations at two different strain levels were analyzed using OVITO software<sup>35</sup> by calculating and visualizing the von Mises strains, simultaneously occurring directional rotation fields, volumetric strains, and strain tensors. All these micromechanical quantities were evaluated for each atom in the system from the relative motion of the neighboring atoms within a cutoff range of 1 nm.

## Results

### Experimental observations

The plane strain distribution can be experimentally determined with high spatial resolution in MGs<sup>28,29,36</sup>. In Fig. 1, we show for the first time the antisymmetric nature of the strain evolution in the MG sample at the notch with unprecedented resolution. As shown in Fig. 1a, c, the elastic strains parallel and perpendicular to the loading direction ( $\varepsilon_{11}$  and  $\varepsilon_{22}$ ) display a highly heterogeneous profile that seems to be stabilized even after releasing the external load. This behavior indicates a highly inhomogeneous deformation mechanism, i.e., shear banding<sup>24,28,29</sup>, and hence, it further confirms that, at low temperatures, the shear bands are the plastic carriers in MGs. HAADF-STEM images of randomly selected areas along the shear fronts of the highest volumetric strain and between the notch area highlight shear band activity (Fig. 2).

The  $\varepsilon_{11}$  component shows localization of dilatation at the notches and along the two shear fronts that extend away from the notches. Contraction can be observed between the notch area and ahead of the intersection points of the two shear fronts. The  $\varepsilon_{22}$  component shows an inverse trend to  $\varepsilon_{11}$ . The strong variations in the shear strain ( $\varepsilon_{12}$ ) further highlight the presence of a complex interpenetrating network of shear bands (Fig. 1b)<sup>28</sup>. Variations in the elastic strain, from compressive to tensile strains, are not only present across the two shear fronts but also can be seen between the notches. The latter Eigenvector evaluation also allows the determination of volumetric strains (free volume) (Fig. 1d). The lowest volumetric strain can be seen at the intersection point of the two shear fronts, where a high density of shear bands concentrates and shows an ascending gradient toward the two notches.

The variations in the Eigenvectors of the strain tensor indicate the direction of the principal strain axes and allow for the localization of shear bands in MGs<sup>37</sup>. The Eigenvectors exhibit an antisymmetric sigmoidal profile consisting of large angular variation at the position of SBs. The evaluation of the Eigenvectors in Fig. 3 highlights a turbulent strain distribution with localization of these turbulent areas close to the notches and along the shear fronts. This turbulent strain distribution correlates to the change in the sign of the strain from compressive to tensile strain. The sigmoidal profile is stronger at the position of the two main shear fronts, but weaker variations in the sign of the strain can be also observed between the notches, highlighting the presence of shear activity.

To distinguish between structural and stress fluctuations in the extremely deformed MG sample, hardness mapping over half of the sample was performed with microindentation. The hardness map indicates a

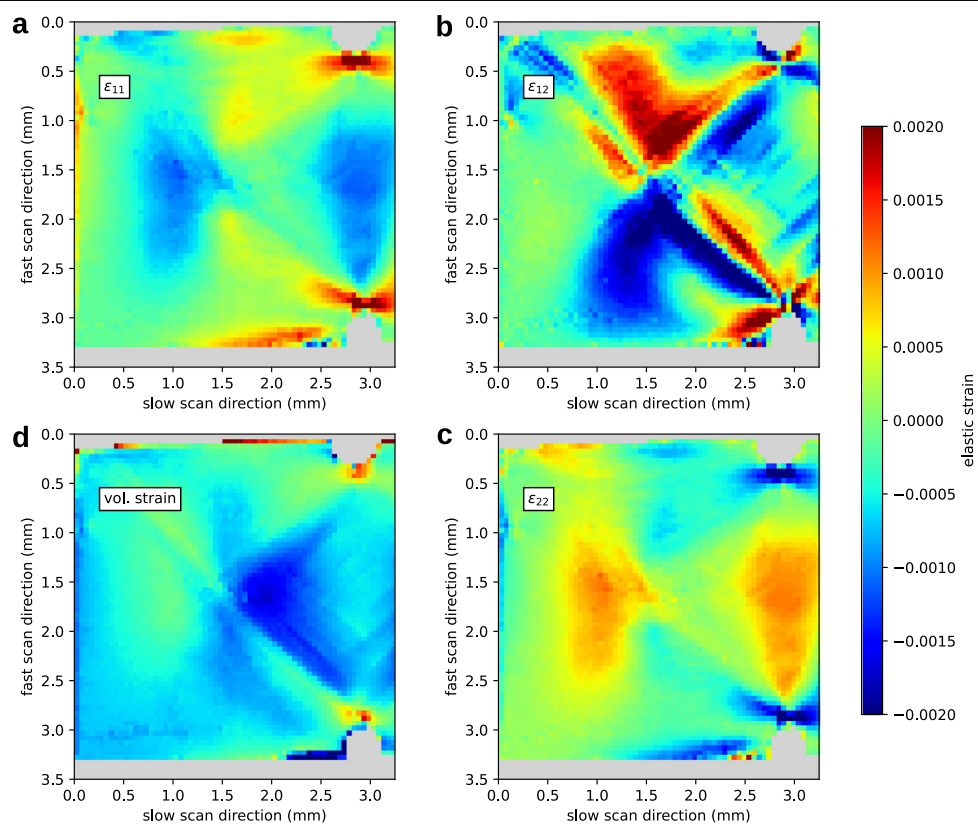


**Fig. 1** Plane strain distribution in  $\text{Zr}_{61}\text{Ti}_2\text{Cu}_{25}\text{Al}_{12}$  MGs after triaxial compression deformation to 40% engineering strain. The deviatoric plane strains **a**  $\varepsilon_{11}$ , **b**  $\varepsilon_{12}$ , and **c**  $\varepsilon_{22}$  determined from the ellipticity of the first amorphous diffraction maximum. **d** The volumetric strain  $\Delta q/\Delta q_1$  is represented to show the change in free volume.

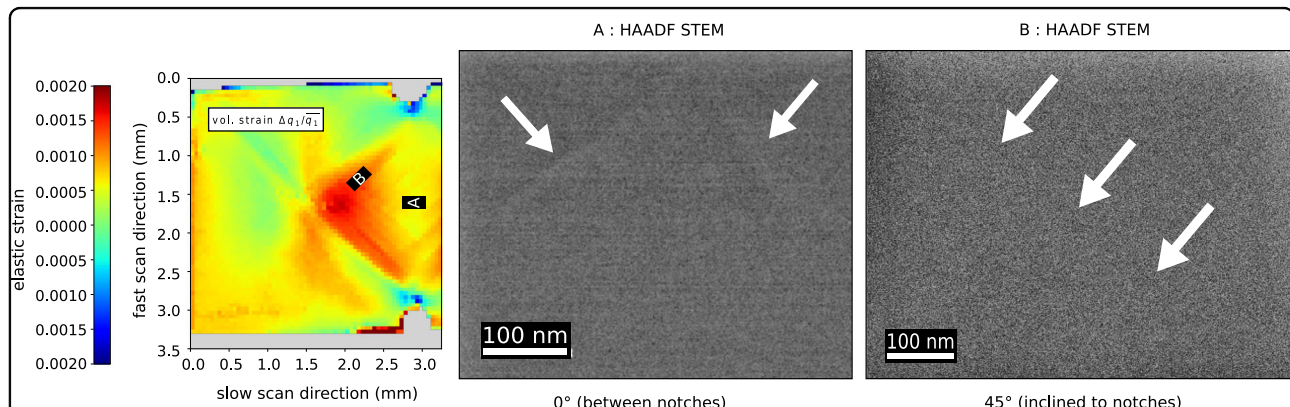
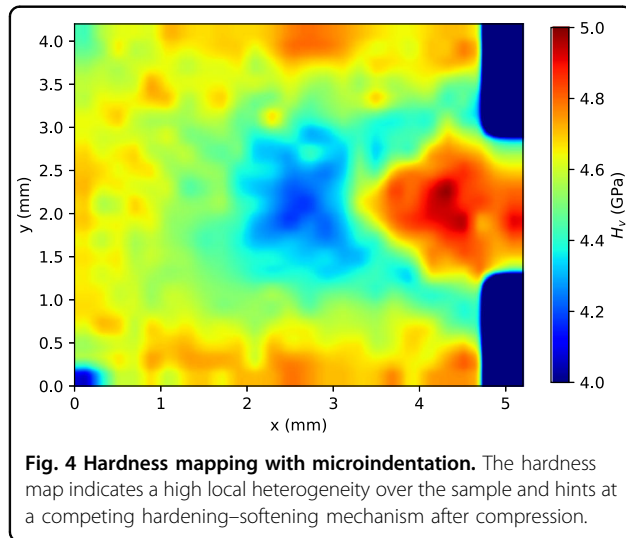
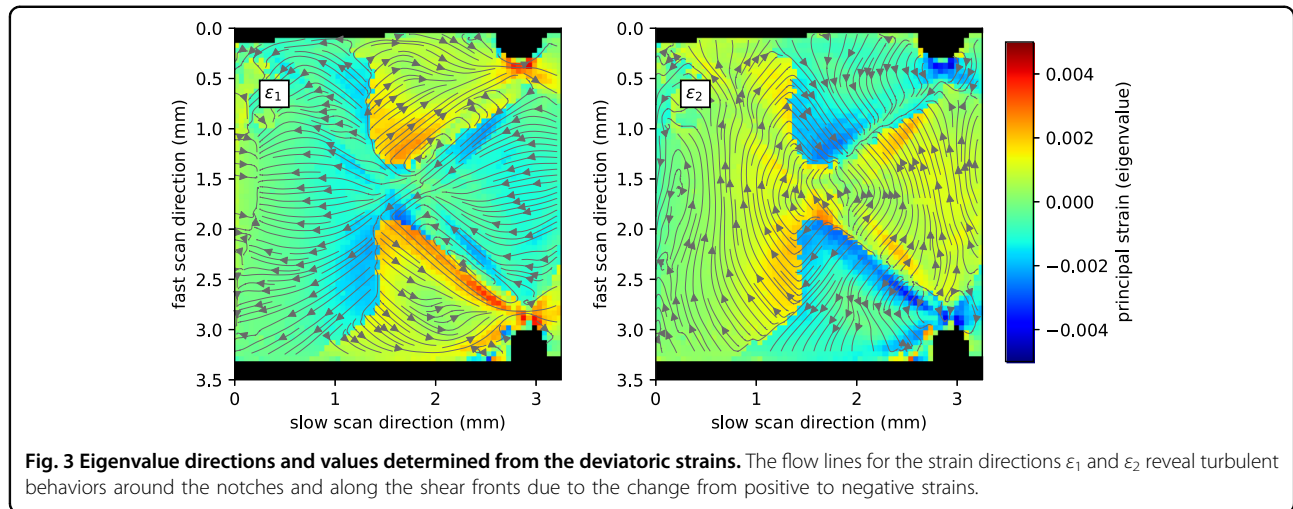


**Fig. 2** HAADF-STEM images of two randomly selected areas. Two HAADF-STEM images are taken from lamellae with a thickness of 100 nm between the notch area and along the shear front (black rectangles marked with **A** and **B** in the volumetric strain map). For each cross-section, HAADF-STEM images show alternating contrast changes, which are related to the presence of shear bands in the material. Arrows pointing at the shear bands provide guidance for the eye.

pronounced local heterogeneity across the sample (Fig. 4). The hardness is expected to decrease monotonically with increasing free volume<sup>38</sup>. Nevertheless, the reduced hardness does not correlate to the low volumetric strain

observed at the intersection point of the two shear fronts with the highest contraction (Fig. 1d). The only reasonable explanation for such a questionable hardness mapping can be the intense shear activity (shear softening)



that overcompensates the presence of residual compressive stresses. However, below the two shear fronts where the volumetric strain is still low, relative to the undeformed sample, the hardness shows the highest values. Here, the shear activity decreases, and the hardness correlates to the compressive stress accumulation. Such behavior can predict that in addition to the structural fluctuations (free volume), the deviatoric strains (stress heterogeneities) may also play a major role in the hardness behavior and in the general mechanical properties of MGs<sup>20</sup>.

#### Atomistic simulations

MD simulations are used to provide an atomistic understanding of the confined deformation mechanisms in a notched MG. In the present case, we aim to distinguish between the structural variations in shear bands and

long-range stress fluctuations between the shear bands. Our approach is to model the deformation under compression of a simplified rectangular sample with two notches (Fig. 5). When the yield commences, four shear fronts initiate from the two notches. For a closer comparison to the experimental setup, only half of the system is shown, and the two shear bands are highlighted by the atomic strain in the upper panel of Fig. 5a. During loading, the two shear bands become dominant and define the shear directions. These two shear bands intersect and block each other, and none transect the entire sample. A better view of the shear band interaction mechanism is given by the sign of the rotation angle, which is generally used to identify vortex-like, rotating units in glassy structures (Fig. 5b)<sup>32,33</sup>. The sign of the rotation defines the shear direction and has a high implication on the dynamics of the shear band interaction. When two shear bands intersect, vortexes of opposite rotation directions come into contact, and the further movement of the shear bands is hindered<sup>33</sup>. This process prevents further shearing and changes the shear band dynamics and morphology, ultimately leading to shear band blocking<sup>32</sup>. The shear band blocking process is particularly important because it plays a decisive role in enhancing the plasticity of MGs and can explain the observed extreme rejuvenation in MGs deformed under triaxial compression<sup>6</sup>.

Structural variation is not only confined to narrow shear bands. When analyzing the volumetric strain, one can see that the local density decreases at the position of the shear bands, which is a consequence of shear softening originating from shear-induced dilatation (Fig. 5c). Moreover, the entire area at the notches, between the four shear fronts, shows relatively large variations with respect to the structure away from the notches. The interpenetrating shear band network confines the material between the shear bands, and the volumetric strain decreases in this

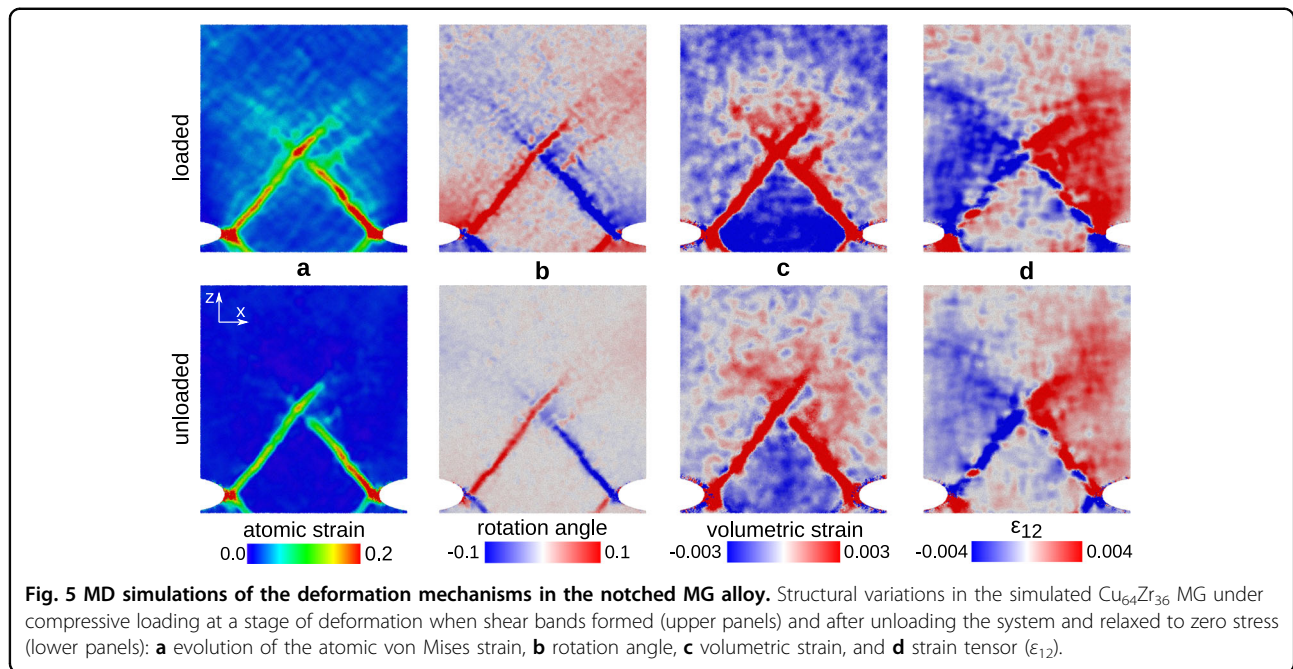


**Fig. 5** MD simulations of the deformation mechanisms in the notched MG alloy. Structural variations in the simulated Cu<sub>64</sub>Zr<sub>36</sub> MG under compressive loading at a stage of deformation when shear bands formed (upper panels) and after unloading the system and relaxed to zero stress (lower panels): **a** evolution of the atomic von Mises strain, **b** rotation angle, **c** volumetric strain, and **d** strain tensor ( $\epsilon_{12}$ ).

region under further compression. MD simulations support the experimental observation and indicate a quantitative comparison between measured and computed volumetric strain values (Fig. 1c and Fig. 5c). Furthermore, when analyzing the strain tensor ( $\epsilon_{12}$ ) distribution obtained from experiments (Fig. 1b) and MD simulations (Fig. 5d), a striking resemblance can be observed. The variation in the elastic strain from compressive to tensile closely follows the shear band fronts. The experimental observations corroborated by MD simulations confirm the presence of intense shearing activity in MGs deformed under triaxial compression.

To distinguish between plastic and elastic strains and highlight the presence of residual stresses in the confined deformation process, the system was unloaded to zero stress (Fig. 5, lower panels). The first important observation is the relaxation of the atomic strain away from the shear bands (Fig. 5a). This phenomenon confirms that structural rejuvenation only correlates to the formation of localized shear bands. The relaxation of the elastic strain is equivalent to a decrease in the rotation field that is mostly observed along the shear bands (Fig. 5b). The second important observation is the relatively low volumetric strain (decreased free volume) between the intersecting shear bands. When the material is confined between shear bands, the residual compressive stress, mirrored to the negative volumetric strain, is not completely relieved after the relaxation process (Fig. 5c). The confined deformation and shear band intersection is further highlighted by the strong variations in  $\epsilon_{12}$  (Fig. 5d).

One should note the differences between the magnitude of the measured parameters in the experiments and

simulations. The quantitative discrepancies result from the large gap between the accessible nm scale in MD simulations and the mm scale in experiments. The length scale limitation of MD is mirrored in the formation of one shear band along each shear front. In the much larger experimental setup, the deformation is mediated by many shear bands. The resolution of the high-energy scanning X-ray diffraction strain mapping is much larger than the width of individual shear bands, and the measured parameters are averaged values. Regardless of the differences between the size and time scales of the simulations and experiments, the simulation results allow for gaining insight into the shear band intersection phenomenon and the atomistic aspects of the rejuvenation process in notched MGs.

## Discussion

From the above results, it can be stated that triaxial deformation of MGs induces both plane (directional) and deviatoric (volumetric) strains. Hence, the reason for the observed extreme rejuvenation corresponds to both structural softening (shear bands) and residual stresses imparted during the deformation process. Additionally, stress heterogeneity is strongly modulated and correlated with the intense shear band activity, as indicated by the shear fluctuations (change in the sign from positive to negative) in the area between the two notches (Fig. 1). It is accepted that shear banding is confined to a narrow thin layer of approximately 20 nm and can extend over a long-range (tens of micrometers) across the shear band<sup>37,39,40</sup>. Experimental observations of high-energy XRD across an individual shear band reveal that the strain at opposite

sides of a shear band changes signs from compressive to tensile<sup>24,29,37</sup>. Likewise, the strains/stresses are created in an inhomogeneous manner during triaxial compression (Fig. 1). Moreover, these fluctuations occur even after unloading, cutting, and polishing the highly deformed sample. Previously, it has been stated that residual stresses are released after the small sample is machined within the notches of a predeformed rod<sup>21</sup>. In their work<sup>21</sup>, the degree of rejuvenation was quantified using the exothermic heat of relaxation ( $\Delta H_{\text{rel}}$ ). Recent results have shown that structurally stable glass can be rejuvenated by decreasing the mechanical stability of its potential energy basin without changing  $\Delta H_{\text{rel}}$ <sup>41</sup>. Furthermore, the measured  $\Delta H_{\text{rel}}$  is mainly related to structural changes, and only a small fraction of this energy corresponds to residual stresses<sup>19</sup>. Consequently, the contributions of stress heterogeneity/fluctuations and residual stresses to rejuvenation and strain hardening have been underestimated<sup>21</sup>. Nevertheless, the presence of residual stresses is reflected in the observed large change in density that exceeds 0.2% (Fig. 1)<sup>42,43</sup>. Indeed, the relative change in density as a function of the cooling rate is usually lower than 0.07%<sup>44,45</sup>. Similar variations in density have been found in cold-rolled MGs<sup>46</sup>. Large variations in density reaching 0.16% have been observed in heavily deformed MGs<sup>47</sup>. In this case, the density fluctuations correspond to enhanced disorder (structural rejuvenation) and the stress constraint introduced by the residual stresses. The effects of residual stresses after mechanical loading are especially important when considering that they can overcompensate or undercompensate the softening caused by shear banding and free volume generation<sup>27,48</sup>. These competing effects may help to explain why the hardness map does not perfectly correlate to the volumetric strain (free volume), especially at the position between the two notches (Fig. 1c). At the intersection point of the two shear fronts, the hardness shows the lowest values, but in contrast, the volumetric strain is low (Fig. 4). As observed in the MD simulations, at this point, there is a strong competition between shear softening and residual compressive stress accumulation. Shear dilatation enhances the free volume, while compressive stress decreases it. However, the hardness depends on both the free volume and local atomic ordering. During shearing, although free volume generation is compensated by the compressive stress buildup, the shearing process breaks the atomic bonds and locally enhances the degrees of disorder. Below the two shear fronts where the shear activity diminishes, the residual compressive stress (low free volume) becomes dominant, and a relatively high hardness is observed. A lower free volume is equivalent to stronger interatomic bonds. Consequently, the contact pressure underneath the indent that is needed to initiate the yield significantly increases in these regions of low volumetric strain<sup>23,49,50</sup>.

## Conclusions

In conclusion, this research has significantly advanced our understanding of MG rejuvenation under constrained deformation protocols. Based on high-energy scanning X-ray diffraction strain mapping, STEM, and micro-indentation analyses, structural and elastic fluctuations, which are the two key factors for the observed extreme rejuvenation in triaxial compression, can be distinguished. STEM characterizations and MD simulations prove that structural rejuvenation under room temperature deformation is related to shear-induced softening and dilatation (large volumetric strain). Additionally, an interpenetrating network of multiple shear bands results in confined plasticity, large variations in the elastic strain, and local accumulation of residual stresses. High-energy scanning X-ray diffraction strain mapping reveals large elastic fluctuations corresponding to the intense shear band activity. The complex superimposed spatial stress and structural heterogeneities reflect the weak correlation between hardness and structural softening and support the competing hardening–softening mechanism. Hence, the classical description of rejuvenation should be reconsidered, and future focus should be given to stress-driven modulation. Stress and structure modulation can be used simultaneously to enhance rejuvenation beyond the limits known to date, thus helping to design MGs with enhanced ductility and strain-hardening capability.

## Acknowledgements

The authors acknowledge financial support from the Deutsche Forschungsgemeinschaft (DFG) through Grant No. SO 1518/1-1, the European Research Council under the ERC Advanced Grant INTELHYB (grant ERC-2013-ADG-340025), Austrian Science Fund (FWF): Y1236-N37, the China Scholarship Council (CSC, 201806220096), the National Natural Science Foundation of China (No. 52171159) and the Natural Science Foundation of Shanghai (No. 22ZR1422500). We acknowledge the European Synchrotron Radiation Facility (ESRF) for providing synchrotron radiation facilities, and we would like to thank Dr. Carlotta Giacobbe for assistance and support in using beamline ID11. Calculations for this research were conducted on the Lichtenberg high-performance computer of the Technische Universität Darmstadt.

## Author details

<sup>1</sup>Erich Schmid Institute of Materials Science, Austrian Academy of Sciences, Jahnstraße 12, 8700 Leoben, Austria. <sup>2</sup>Institut für Materialwissenschaft, Fachgebiet Materialmodellierung, Technische Universität Darmstadt, Otto-Beindt-Straße 3, 64287 Darmstadt, Germany. <sup>3</sup>Department of Materials Science, Chair of Materials Physics, Mountain University Leoben, Jahnstraße 12, 8700 Leoben, Austria. <sup>4</sup>Laboratory for Microstructures, Institute of Materials, Shanghai University, 200444 Shanghai, China. <sup>5</sup>European Synchrotron Radiation Facility (ESRF), 38042 Grenoble, France. <sup>6</sup>Laboratory of Metal Physics and Technology, Department of Materials, ETH Zurich, 8093 Zurich, Switzerland

## Author contributions

D.S. wrote the original draft. D.S., F.S. and X.B. designed the research. F.S., J.W. and M.S. performed the synchrotron experiments. D.S. and F.S. evaluated and cured the data. S.F. and M.G. performed the microindentation experiments. S.F. and C.G. performed the STEM experiments. X.B. produced the alloy and compression tests. D.S. performed the MD simulations. J.E. and G.W. provided funding. All authors contributed to the interpretation of the data and revised the manuscript.

**Data availability**

The data generated during this study are available from the corresponding author upon request.

**Code availability**

The open-source computer code LAMMPS used in this study was developed and maintained at Sandia National Laboratories. LAMMPS is available at <https://lammps.sandia.gov>.

**Conflict of interest**

The authors declare no competing interests.

**Publisher's note**

Springer Nature remains neutral with regard to jurisdictional claims in published maps and institutional affiliations.

**Supplementary information** The online version contains supplementary material available at <https://doi.org/10.1038/s41427-023-00509-5>.

**Received: 9 May 2023 Revised: 12 October 2023 Accepted: 20 October 2023.**

**Published online: 24 November 2023**

**References**

- Isner, B. A. & Lacks, D. J. Generic rugged landscapes under strain and the possibility of rejuvenation in glasses. *Phys. Rev. Lett.* **96**, 025506 (2006).
- Fan, Y., Iwashita, T. & Egami, T. Energy landscape-driven non-equilibrium evolution of inherent structure in disordered material. *Nat. Commun.* **8**, 15417 (2017).
- Saida, J., Yamada, R. & Wakeda, M. Recovery of less relaxed state in Zr-Al-Ni-Cu bulk metallic glass annealed above glass transition temperature. *Appl. Phys. Lett.* **103**, 221910 (2013).
- Küchermann, S. et al. Energy storage in metallic glasses via flash annealing. *Adv. Funct. Mater.* **28**, 1805385 (2018).
- Wakeda, M., Saida, J., Li, J. & Ogata, S. Controlled rejuvenation of amorphous metals with thermal processing. *Sci. Rep.* **5**, 1–8 (2015).
- Pan, J. et al. Extreme rejuvenation and softening in a bulk metallic glass. *Nat. Commun.* **9**, 1–9 (2018).
- Park, K. W., Wakeda, M., Shibutani, Y., Fleury, E. & Lee, J. C. Effect of the atomic packing density on the structural change rate of amorphous alloys under elastostatic stress. *Met. Mater. Int.* **14**, 159163 (2008).
- Concstell, A., Mérat, F. O., Surinach, S., Baró, M. D. & Greer, A. L. Structural relaxation and rejuvenation in a metallic glass induced by shot-peening. *Philos. Mag. Lett.* **89**, 831–840 (2009).
- Dmowski, W. et al. Structural rejuvenation in a bulk metallic glass induced by severe plastic deformation. *Acta Mater.* **58**, 429–438 (2010).
- Ding, G. et al. Ultrafast extreme rejuvenation of metallic glasses by shock compression. *Sci. Adv.* **5**, 6249 (2019).
- Feng, S. et al. Rejuvenation by weakening the medium range order in  $Zr_{46}Cu_{44}Al_8$  metallic glass with pressure preloading: a molecular dynamics simulation study. *Mater. Des.* **158**, 248–255 (2018).
- Mahmoud, Z. H. et al. Identification of rejuvenation and relaxation regions in a Zr-based metallic glass induced by laser shock peening. *J. Mater. Res. Technol.* **11**, 2015–2020 (2021).
- Liu, J. W., Cao, Q. P., Chen, L. Y., Wang, X. D. & Jiang, J. Z. Shear band evolution and hardness change in cold-rolled bulk metallic glasses. *Acta Mater.* **58**, 4827–4840 (2010).
- Ge, T. et al. Unusual energy state evolution in Ce-based metallic glass under high pressure. *J. Appl. Phys.* **121**, 205109 (2017).
- Wang, C. et al. High stored energy of metallic glasses induced by high pressure. *Appl. Phys. Lett.* **110**, 111901 (2017).
- Miyazaki, N., Wakeda, M., Wang, Y. J. & Ogata, S. Prediction of pressure-promoted thermal rejuvenation in metallic glasses. *Npj Comput. Mater.* **2**, 1–9 (2016).
- Deng, C. & Schuh, C. A. Atomistic mechanisms of cyclic hardening in metallic glass. *Appl. Phys. Lett.* **100**, 251909 (2012).
- Zhao, D., Zhao, H., Zhu, B. & Wang, S. Investigation on hardening behavior of metallic glass under cyclic indentation loading via molecular dynamics simulation. *Appl. Surf. Sci.* **416**, 14–23 (2017).
- Stolpe, M., Kružic, J. J. & Busch, R. Evolution of shear bands, free volume and hardness during cold rolling of a Zr-based bulk metallic glass. *Acta Mater.* **64**, 231–240 (2014).
- Zhang, Y., Wang, W. H. & Greer, A. L. Making metallic glasses plastic by control of residual stress. *Nat. Mater.* **5**, 857–860 (2006).
- Pan, J., Ivanov, Y. P., Zhou, W. H., Li, Y. & Greer, A. L. Strain-hardening and suppression of shear-banding in rejuvenated bulk metallic glass. *Nature* **578**, 559–562 (2020).
- Ustundag, E. et al. Residual stresses in bulk metallic glasses due to differential cooling or thermal tempering. *MRS Online Proc. Libr.* **554**, 431–436 (1998).
- Wang, L., Bei, H., Gao, Y. F., Lu, Z. P. & Nieh, T. G. Effect of residual stresses on the hardness of bulk metallic glasses. *Acta Mater.* **59**, 2858–2864 (2011).
- Kosiba, K. et al. Guiding shear bands in bulk metallic glasses using stress fields: A perspective from the activation of flow units. *Phys. Rev. B* **102**, 134113 (2020).
- Haag, F., Beitzschmidt, D., Eckert, J. & Durst, K. Influences of residual stresses on the serrated flow in bulk metallic glass under elastostatic four-point bending—a nanindentation and atomic force microscopy study. *Acta Mater.* **70**, 188–197 (2014).
- Wang, J.-Q. et al. Rapid degradation of azo dye by Fe-based metallic glass powder. *Adv. Funct. Mater.* **22**, 2567–2570 (2012).
- Yuan, X., Şopu, D. & Eckert, J. Origin of strain hardening in monolithic metallic glasses. *Phys. Rev. B* **103**, L140107 (2021).
- Shakur Shahabi, H. et al. Mapping of residual strains around a shear band in bulk metallic glass by nanobeam X-ray diffraction. *Acta Mater.* **111**, 187–193 (2016).
- Scudino, S. Mechanism of shear banding during cold rolling of a bulk metallic glass. *J. Alloy. Compd.* **773**, 883–889 (2019).
- Plimpton, S. Fast parallel algorithms for short-range molecular-dynamics. *J. Comput. Phys.* **117**, 1–19 (1995).
- Mendelev, M. I., Sordelet, D. J. & Kramer, M. J. Using atomistic computer simulations to analyze X-ray diffraction data from metallic glasses. *J. Appl. Phys.* **102**, 043501 (2007).
- Şopu, D., Scudino, S., Bian, X. L., Gammer, C. & Eckert, J. Atomic-scale origin of shear band multiplication in heterogeneous metallic glasses. *Scr. Mater.* **178**, 57–61 (2020).
- Şopu, D. et al. From elastic excitations to macroscopic plasticity in metallic glasses. *Appl. Mater. Today* **22**, 100958 (2021).
- Moitzi, F. et al. Chemical bonding effects on the brittle-to-ductile transition in metallic glasses. *Acta Mater.* **188**, 273–281 (2020).
- Stukowski, A. Visualization and analysis of atomistic simulation data with ovito—the open visualization tool. *Modell. Simul. Mater. Sci. Eng.* **18**, 015012 (2010).
- Binkowski, I. et al. Sub-micron strain analysis of local stick-slip motion of individual shear bands in a bulk metallic glass. *Appl. Phys. Lett.* **107**, 221902 (2015).
- Scudino, S. & Şopu, D. Strain distribution across an individual shear band in real and simulated metallic glasses. *Nano Lett.* **18**, 1221–1227 (2018).
- Yoo, B.-G., Kim, Y.-J., Oh, J.-H., Ramamurty, U. & Jang, J.-I. On the hardness of shear bands in amorphous alloys. *Scr. Mater.* **61**, 951–954 (2009).
- Maaß, R., Kläumünzer, D. & Löffler, J. F. Propagation dynamics of individual shear bands during inhomogeneous flow in a Zr-based bulk metallic glass. *Acta Mater.* **59**, 3205–3213 (2011).
- Liu, C. & Maaß, R. Elastic fluctuations and structural heterogeneities in metallic glasses. *Adv. Funct. Mater.* **28**, 1800388 (2018).
- Gao, Y. et al. Rejuvenation deformation relationship of a well-aged metallic glass during newtonian to nonnewtonian flow. *J. Non-Cryst. Solids* **615**, 122410 (2023).
- Johnson, W. L. & Samwer, K. A universal criterion for plastic yielding of metallic glasses with a  $(T/T_g)^{2/3}$  temperature dependence. *Phys. Rev. Lett.* **95**, 195501 (2005).
- Wang, W. H. Correlations between elastic moduli and properties in bulk metallic glasses. *J. Appl. Phys.* **99**, 93506 (2006).
- Hu, X., Ng, S. C., Feng, Y. P. & Li, Y. Cooling-rate dependence of the density of  $Pd_{40}Ni_{10}Cu_{30}P_{20}$  bulk metallic glass. *Phys. Rev. B* **64**, 172201 (2001).
- Fu, W., Sun, Y. & Zhang, W. The effect of cooling rate on microstructure and mechanical properties of Zr-based bulk metallic glasses. *Adv. Mater. Sci. Eng.* **2013**, 826758 (2013).
- Haruyama, O. et al. Characterization of free volume in cold-rolled  $Zr_{55}Cu_{30}Ni_5Al_{10}$  bulk metallic glasses. *Acta Mater.* **61**, 3224–3232 (2013).

47. Vempati, U. K., Valavala, P. K., Falk, M. L., Almer, J. & Hufnagel, T. C. Length-scale dependence of elastic strain from scattering measurements in metallic glasses. *Phys. Rev. B* **85**, 214201 (2012).
48. Launey, M. E., Busch, R. & Kružić, J. J. Effects of free volume changes and residual stresses on the fatigue and fracture behavior of a Zr-Ti-Ni-Cu-Be bulk metallic glass. *Acta Mater.* **56**, 500–510 (2008).
49. Chen, M. W. Mechanical behavior of metallic glasses: microscopic understanding of strength and ductility. *Annu. Rev. Mater. Res.* **38**, 445–469 (2008).
50. Zhu, Y. & Wu, X. L. Perspective on hetero-deformation induced (HDI) hardening and back stress. *Mater. Res. Lett.* **7**, 393–398 (2019).